Measurement of the real dielectric permittivity ϵ_r of glacial ice

Abdul, U.L.[1], Allison, P.[2,3], Archambault, S.[4], Auffenberg, J.[5], Bard, R.[6], Beatty, J.J.[2,3], Beheler-Amass, M.[5], Besson, D.Z.[1,7], Beydler, M.[5], Brabec, C.[1], Chen, C.C.[8], Chen, C.H.[8], Chen, P.[8], Christenson, A.[5], Clark, B.A.[2,3], Connolly, A.[2,3], Cremonesi, L.[9], Deaconu, C.[10], Duvernois, M.[5], Fender, C.[2], Friedman, L.[6], Gaior, R.[4], Hanson, J.[2,3], Hanson, K.[5], Haugen, J.[5], Hoffman, K.D.[6], Hong, E.[2,3], Hsu, S.Y.[8], Hu, L.[8], Huang, J.J.[8], Huang, M.-H. A.[8], Ishihara, A.[4], Karle, A.[5], Kelley, J.L.[5], Khandelwal, R.[5], Kim, M.-C.[4], Kravchenko, I.[11], Kruse, J.[11], Kurusu, K.[4], Kuwabara, T.[4], Landsman, H.[12], Laundrie, A.[5], Li, C.-J.[8], Liu, T.-C.[8], Lu, M.-Y.[5], Mase, K.[4], Meures, T.[5], Nam, J.[4], Nichols, R.J.[9], Nir, G.[12], Novikov, A.[1,7], Oberla, E.[10], O' Murchadha, A.[5], Pan, Y.[13], Pfendner, C.[2,3], Ratzlaff, K.[1], Relich, M.[3], Roth, J.[13], Sandstrom, P.[5], Schellin, P.[2,3], Seckel, D.[13], Shiao, Y.S.[8], Shultz, A.[11], Song, M.[6], Touart, J.[6], Varner, G.S.[14], Vieregg, A.[10], Wang, M.Z.[8], Wang, S.H.[8], Wissel, S.[15], Yoshida, S.[4], and Young, R.[1]

[1]Dept. of Physics and Astronomy, Univ. of Kansas, Lawrence, KS, USA
[2]Dept. of Physics, The Ohio State University, 191 West Woodruff Avenue, Columbus, OH, USA
[3]Center for Cosmology and Astro-Particle Physics, The Ohio State University, 191 West Woodruff Avenue, Columbus, OH, USA
[4]Dept. of Physics, Chiba University, Tokyo, Japan
[5]Dept. of Physics and Wisconsin IceCube Particle Astrophysics Center, University of Wisconsin, Madison, WI, USA
[6]Dept. of Physics, Univ. of Maryland, College Park, MD, USA
[7]National Research Nuclear University, Moscow Engineering Physics Institute, Moscow, Russia
[8]Dept. of Physics, Grad. Inst. of Astrophys., & Leung Center for Cosmology and Particle Astrophysics, National Taiwan Univ., Taipei, Taiwan
[9]Dept. of Physics and Astronomy, Univ. College London, London, United Kingdom
[10]Dept. of Physics, University of Chicago, Chicago, IL, USA
[11]Dept. of Physics and Astronomy, Univ. of Nebraska-Lincoln, NE, USA
[12]Weizmann Institute of Science, Rehovot, Israel
[13]Dept. of Physics and Astronomy, Univ. of Delaware, Newark, DE, USA
[14]Dept. of Physics and Astronomy, Univ. of Hawaii, Manoa, HI, USA
[15]Dept. of Physics, California Polytechnic State University, San Luis Obispo, CA, USA

December 12, 2017

Abstract

Using data collected by the Askaryan Radio Array (ARA) experiment at the South Pole, we have used long-baseline propagation of radio-frequency signals to extract information on the radio-frequency index-of-refraction ($n = \sqrt{\epsilon_r}$) in South Polar ice, comparing the arrival times of directly propagating rays with refracted rays. We also observe indications, for the first time, of radio-frequency ice birefringence for signals propagating along predominantly horizontal trajectories, corresponding to an asymmetry of order 0.1% between the ordinary and extra-ordinary birefringent axes, numerically compatible with previous measurements of birefringent asymmetries for vertically-propagating radio-frequency signals at South Pole.

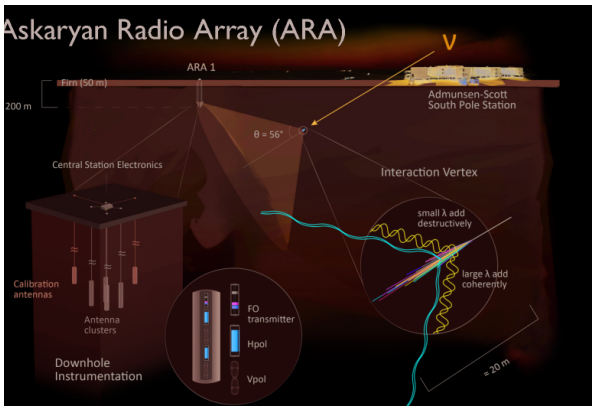

Figure 1: Schematic of ARA neutrino detection, showing the ARA receiver antennas illuminated by radio-frequency Cherenkov signal resulting from an in-ice neutrino interaction.

I. Introduction

The glacial ice at the South Pole offers a unique opportunity for detection of neutrinos. There are currently three Antarctic experiments which seek detection, via the Askaryan effect[1, 2, 3], of ultra-high energy (UHE; $E >$ 10 PeV) neutrinos using the ice sheet as a neutrino target[4]. Hadronic and electromagnetic showers resulting from neutrino collisions with ice molecules acquire, as they evolve, a net negative charge as atomic electrons are Compton scattered into the forward-moving shower and shower positrons depleted via annihilation with atomic electrons, resulting in a coherent, detectable electromagnetic signal at radio wavelength scales, distributed on a Cherenkov cone approximately 1–2 degrees in transverse width. The most promising ("cosmogenic") neutrino source for these experiments[5, 6, 7, 8] results from photoproduction of pions due to interactions of ultra-high energy nucleons with cosmic microwave background (CMB) photons, with subsequent decays to neutrinos.

The Askaryan Radio Array[9, 10, 11] (ARA) at the South Pole (Figure 1) has proposed 37 independent stations in a hexagonal array with inter-station spacing of 2 km. Following the initial 2010/11 deployment of a "TestBed" in the upper 30 meters of the South Polar ice sheet, three more (ARA-1, ARA-2, and ARA-3) stations were deployed in 2011/12 and 2012/13, with three more (ARA-4, ARA-5, and ARA-6), including one with an advanced trigger system exploiting phased array techniques[12], scheduled for deployment during the 2017/18 austral season. Following ARA-1, for which a drill malfunction limited deployment to approximately 40% of the desired 200 meter depth, the subsequent station antennas were deployed at depths of 175-200 m. Each station includes 16 antennas, 8 sensitive to vertically polarized (Vpol) and 8 predominantly sensitive to horizontally polarized (Hpol) radiation, with in-ice bandwidths of approximately 150-700 MHz and 250-400 MHz, respectively. Surface antennas, sensitive over the 25–800 MHz regime, deployed on the TestBed, ARA-1, ARA-2 and ARA-3, can be used to monitor low-frequency galactic noise, although they rarely give signals coincident with the in-ice antennas, given the typical time delays in signal arrival times between the surface and the deep station antennas. In-ice antennas are installed on four strings and define the corners of a cuboid approximately 20m in height and 20m along the horizontal diagonal. An H/V pair is located at each corner of the cuboid, consisting of an Hpol antenna deployed 2m–3m above a Vpol antenna. Signals are amplified at the antenna,

passed by an in-ice RF-over-optical fiber link to the surface, and then converted back to RF voltage signals by a surface optical fiber receiver before entering the data acquisition system. ARA data collection is triggered at a station whenever (3 of 8 Hpol) .OR. (3 of 8 Vpol) antennas exceed some voltage threshold within a time window (170 ns) inclusive to the RF travel time across the station. Thresholds are dynamically adjusted to maintain a constant singles rate, and (approximately) a combined event trigger rate of 5-7 Hz, comfortably below the saturation data-taking rate of 25 Hz. Following the issue of a valid trigger, signals from all 16 antennas are digitized and stored, with a readout window typically wide enough to include ∼100 ns of pre-trigger and ∼300 ns of post trigger waveform.

Similar to ARA, ARIANNA[13], located on the Ross Ice Shelf, features an isolated, radio-quiet site with log-periodic dipole antennas deployed on the surface. Downward-pointing antennas search for upcoming Askaryan signal generated by neutrino interactions in the ice; upward-pointing antennas have been used to measure down-coming Askaryan-like signals generated by charged cosmic rays interacting in the Earth's atmosphere[14]. The ANITA experiment[15] features a suite of radio-frequency horn antennas suspended from a balloon flying at an elevation of 38 km in a circumpolar orbit over the Antarctic continent, scanning for upcoming radio signals resulting from charged cosmic ray or neutrino interactions.

In this paper, we analyze calibration data taken with the ARA stations with the goal of putting constraints on the ice dielectric permittivity in the radio-frequency regime.

II. Geometric Optics and Ray tracing

The sensitivity of any neutrino-search experiment such as ARA depends on a) the degree of signal absorption in the target ice medium (determined by the imaginary component of the ice dielectric permittivity), and b) the volume of ice 'visible' to the radio receiver array (determined by the real component of the ice dielectric permittivity). The absorption length for RF signals in the frequency range of interest (100–1000 MHz) has been measured to exceed 1 km in the upper 1.5 km of the South Polar ice sheet, making it an ideal medium for neutrino detection[16]. However, the changing density of the ice results in a group velocity varying monotonically with depth. In such a case, Fermat's Least-time principle implies that a) rays will follow curved paths, and b) there may be regions which are 'shadowed', for which the superposition of all contributing rays gives zero net amplitude. Moreover, there may be multiple signals observed from a single source, resulting from either continuous refraction through the ice itself, or reflection from the upper ice/air interface as illustrated in Figure 2.

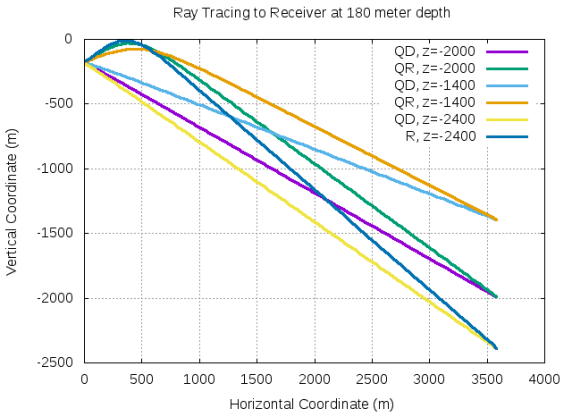

Figure 2: Simulation of ray tracing assuming ARA index-of-refraction profile with depth, showing trajectories of Quasi-Direct (QD) and Quasi-Refracted (QR) rays as a function of lateral distance (x, in meters) and vertical distance (z, in meters). Refracted and direct rays are typically separated by approximately 40 degrees at the measurement point with corresponding launch angles at the source separated by ∼5 degrees. Note shadow zones in upper right of plot.

The index-of-refraction should itself roughly scale with the local ice density.

Robin suggested the parameterization n(z)=1+0.86$\rho(z)$[17] based on a clever interferometric technique, in which signals recorded on the surface from a transmitter lowered into a Devon Island ice bore hole were mixed with a fixed frequency; the wavelength of the ice at the depth of the transmitter was then inferred from the measured beats. Similar parameterizations can be found elsewhere (n(z)=0.992+0.848$\rho(z)$, e.g., as determined from a fit to McMurdo Sound ice measurements[18]), although not all obey the contraint that n(z)$\rightarrow$1 in the limit of ρ=0. Fig. 3 overlays density data[19, 20], and direct index-of-refraction measurements made at the South Pole with the 'best-fit' profile used by the ARA experiment as well as two other alternate forms. We note that the density data show considerable deviations from smoothness, which could, in principle, result in sub-dominant 'channeling' effects. This possibility is especially interesting in the context of reports of horizontal propagation of RF signals emanating from within the 'shadow zone' expected in the presence of a gradient to the index of refraction[21, 22]. Such propagation could occur if there are density layers in the firn. A density inversion could produce a horizontal waveguide where radiation is confined by refraction, similar to an optical fiber with a graded index of refraction. Similarly, weak discontinuities in density can result in scattering surfaces for highly inclined rays, producing a "channel" for horizontal propagation.

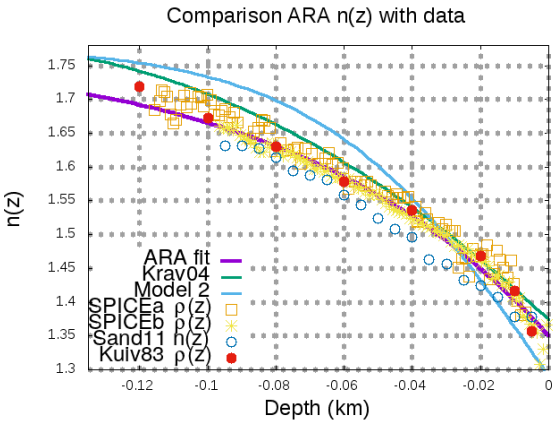

Figure 3: Compilation of index-of-refraction vs. depth data (points) overlaid with the ARA n(z) model. Data are culled from density measurements made by Kuivinen *et al* [19] and two SPICE cores extracted in 2015[23], and converted to index-of-refraction using n(z)=1+0.86$\rho(z)$, as well as direct n(z) measurements by one of the authors ("Sand11") using a co-lowered transmitter/receiver pair, based on propagation time information.

i. Probes of index-of-refraction profile n(z) using ARA data

In the middle of the expected cosmogenic neutrino energy spectrum ($E_\nu \sim 10^{18.5}$ eV), ARA is designed to detect sources several km distant. It is therefore critical to understand the properties of the ice within the array, especially at the 1-2 km depths corresponding to the interval over which the bulk of detectable neutrinos are expected to interact. Anticipating this, during the last year (2010-11) of IceCube construction, two pulsers were deployed on IceCube string 1 ("ICS1") at depths z=-1400 m and z=-2450 m, and one on IceCube string 22 ("ICS22") at a depth z=-1400 m, proximal to the planned ARA. The pulser at 2450 m depth was operated in conjunction with the ARA TestBed to validate the South Pole index of refraction profile with depth n(z) and also the RF attenuation dependence on depth[9], but failed within the first year of operation. The pulsers ("ICS1", "ICS22") at depths of 1400 m were operated in 2014/15 as part of the calibration of ARA-2 and ARA-3, and again in 2016/17 after the ARA-2 trigger timing and readout window was adjusted, enabling capture of an extended waveform. The ARA-3 array was inoperable at the time of the 2017 data-taking.

Given the monotonic increase of n(z) with depth over the upper 150 meters of the ice sheet, the presence of two rays from source to receiver is generic for our geometry (Fig. 2), with a quasi-direct (QD) ray typically upcoming at the station and either a reflected or

a quasi-reflected ray ("QR", cresting prior to "true" reflection at the upper surface) downgoing. The maximum in-ice height of the QR ray can be determined from Snell's law and either the launch angle of the ray at the source, or the received angle at the station. The time delay between arrival of the QD and the QR rays is of order hundreds of ns; with the exception of the 2016/17 ARA-2 data, this time lag is generally larger than the waveform capture window. The observed QD/QR time delays can, in turn, be used to discriminate between putative n(z) models. Several functional n(z) forms were tested against the measured timings. These included:

- Krav04: n(z)=1.37-(4.6z+13.72z^2) for $z >$-0.18 km, as suggested by a polynomial fit to direct radio wavespeed measurements at South Pole[24].
- Model 2: n(z)=0.8+0.98/(1+exp(30z))
- ARA fit: n(z)=1.78-0.43exp(13.2z),

with z in units of km, and increasingly negative with increasing depth. The last two exponential forms match the density dependence expected in a gravitational field. We find that the profile n(z)=1.78-0.43exp(13.2z) currently used in the ARA Monte Carlo simulation provides the minimum χ^2 relative to the measured time differences between the QR and QD rays, observed in experimental data. This functional form also matches the $n_{surface}$(z=0)=1.35 and n_{deep}(z<-0.2)$\rightarrow$1.78 boundary conditions, consistent with density measurements at the South Pole, and also provides the best-fit to the density data. The remainder of the analysis described below therefore assumes this dependence.

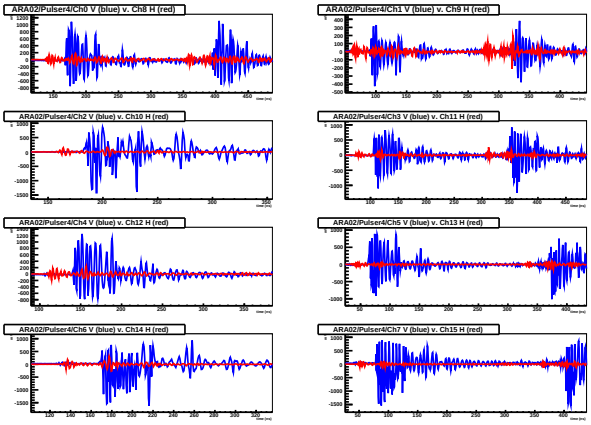

Figure 4: ICS1 waveform captures registered by ARA-2 station showing 16 channels in 8 H/V pairs (blue=VPol [Channels 0–7]; red=HPol [Channels 8–15]).

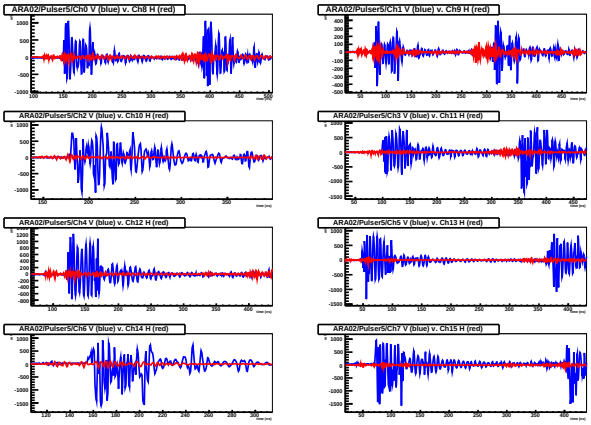

Figure 5: ICS22 waveform captures registered by ARA-2 station showing 16 channels in 8 H/V pairs (blue=VPol [Channels 0–7]; red=HPol [Channels 8–15]).

ii. Analysis of QD and QR rays

Figures 4 and 5 shows deep pulser events which trigger ARA-2 and ARA-3, respectively. The quality of the pulses is visible from the leading edge. The QD rays travel exclusively through deep ice; the sharpness of the leading edge implies relatively little scattering and/or

dispersive effects, consistent with studies of vertical echoes[25]. By contrast, the pulses identified as QR rays indicate a precursor which may be due to scattering in the firn layer near the top of the pulse trajectory.

Using the calibrated station geometry, one can infer the zenith angle of the arriving rays and verify their consistency with the QR/QD hypothesis. As shown in Figure 6, the earlier

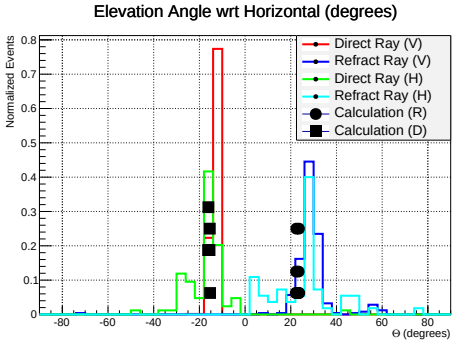

Figure 6: Calculated angle of incidence, relative to horizontal, for ARA-2 2017 deep pulser data.

set of pulses arrive from below the horizontal; the later set of pulses arrive from above the horizontal, consistent with expectations for the QD and QR rays, respectively. Similarly, Fig-

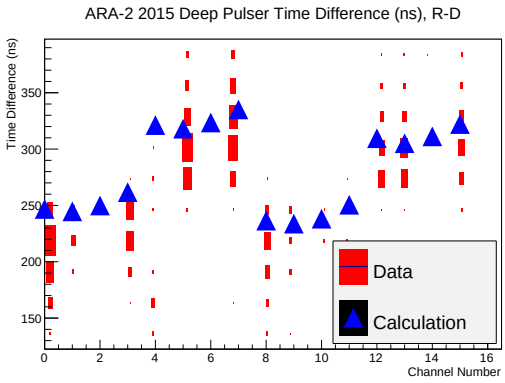

Figure 7: Measured time differences between QD and QR rays for ARA-2 2017 deep pulser data, compared with calculation.

ure 7 compares the calculated, expected time difference between the arrival of the QD and QR rays using our putative n(z) model with data. Given the inherent uncertainty in discerning hit times algorithmically, the two show acceptable agreement.

iii. Angular Source Reconstruction

Source location reconstruction is used to verify the three-dimensional source point using the recorded waveforms. The standard ARA interferometry-based analysis event reconstruction cross-correlates the waveforms (QD_i, QD_j), where QD_i and QD_j are the quasi-direct signals on channels i and j. Through a fast lookup table of calculated, expected arrival times, a set of predicted δt_{ij} (r, θ, ϕ) are produced for every possible source position. These are used to sample the Hilbert envelope of the i−j cross correlation function and give weights to the putative δt_{ij}[26]. For this study, a second table for QR signal arrival times is built, and we extend the cross correlation to include all the available QR signals. Thus, the full reconstruction incorporates contributions from all possible QD−QD, QD−QR, and QR−QR pairs. To improve the experimental precision, each waveform used was individually visually scanned. We inspect data from each pulser separately, visually identify rising edges for the signals, and capture 50 ns pre-edge plus 150 ns post-edge data to form a 200ns-long waveform for each QD/QR ray. Cross-correlation envelopes are then calculated using these shortened waveforms. We note that this optimized procedure obviously is not applicable generally, but is tractable for this small-event sample. For each putative source position, we compute the sum of the envelope functions across all pairs of signals in the event, and the maximum of these "coherence" values determines the most-likely position. A source location map of a deep pulser event is show in Figure 8; the brightest $1^\circ \times 1^\circ$ pixel in that map is identified as the best-fit source position. The distribution of reconstructed deep pulser directions, as defined by the maximum intensity pixel in each event, is presented in Figures 9, 10, 11 and 12. In general, we reconstruct the source direction with an error of order one degree in both azimuth and elevation.

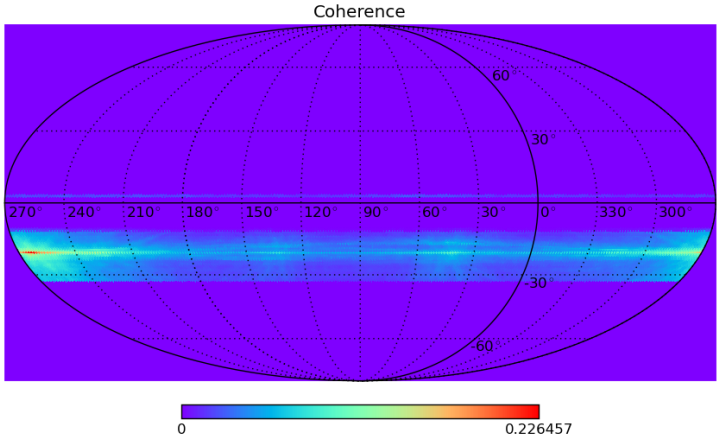

Figure 8: Reconstructed interferometric image of ARA ICS22 deep pulser, using standard azimuth (horizontal) vs. zenith (i.e., elevation [vertical]) coordinates. Highest intensity pixel is visible in lower left.

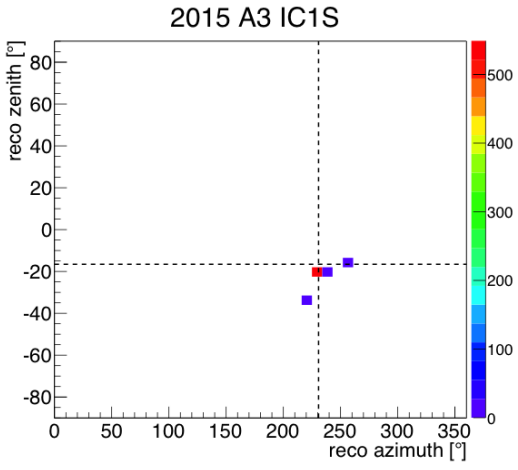

Figure 9: ARA-3 azimuthal (ϕ) vs. zenith (θ) reconstructed source locations during time when ICS1 was pulsing. Dashed lines indicate "true" source location.

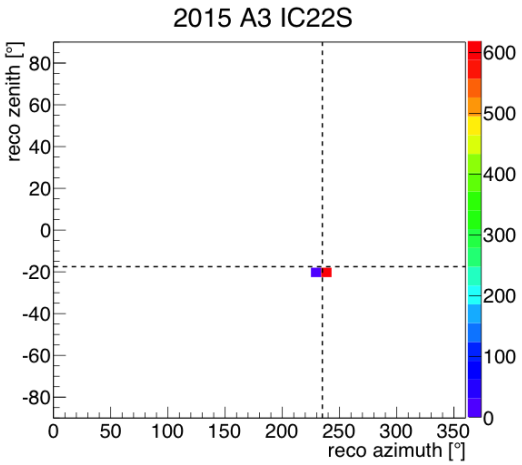

Figure 10: ARA-3 azimuthal (ϕ) vs. elevation (θ) reconstructed source locations during time when ICS22 was pulsing.

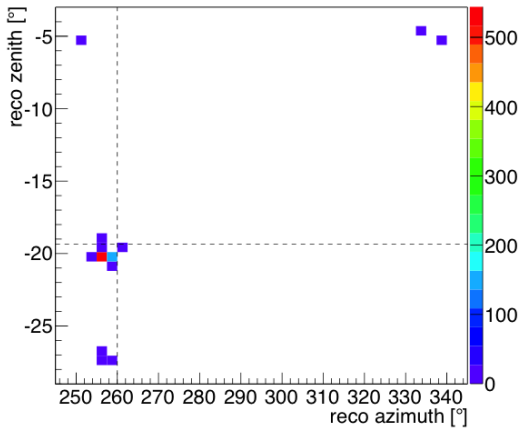

Figure 11: ARA-2 azimuthal (ϕ) vs. zenith (θ) reconstructed source locations during time when ICS1 was pulsing.

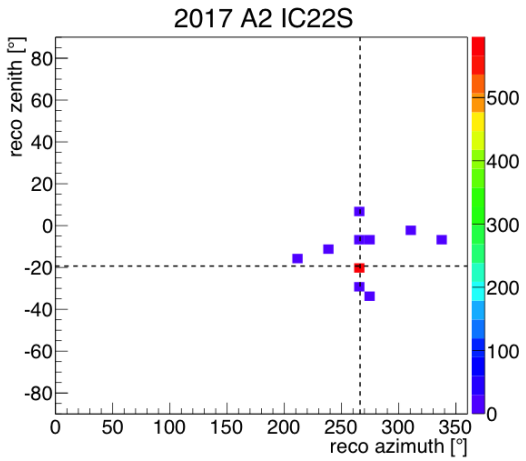

Figure 12: ARA-2 azimuthal (ϕ) vs. zenith (θ) reconstructed source locations during time when ICS22 was pulsing.

iv. Range Reconstruction

The reconstruction from QD rays permits a good direction to the vertex, but determining the distance to the vertex is more difficult, as this requires a determination of the curvature of the radiation front, which is limited by the modest 20 m baseline of the station. In the present case, however, comparison of the QD with the QR signal arrival times allows improved estimation of range-to-vertex. Considering the quasi-reflected ray as if it were detected by an "image" station above the ice surface, the baseline for reconstruction by both rays is of order twice the depth of the station, or 400m, enabling a full 3D reconstruction. The results of this exercise are presented in Figures 13 and 14 for ARA-2 reconstruction of the ICS1 and ICS22 pulsers. Deviations in elevation reconstruction of order one degree typically translate into range errors of tens of percent. Table 1

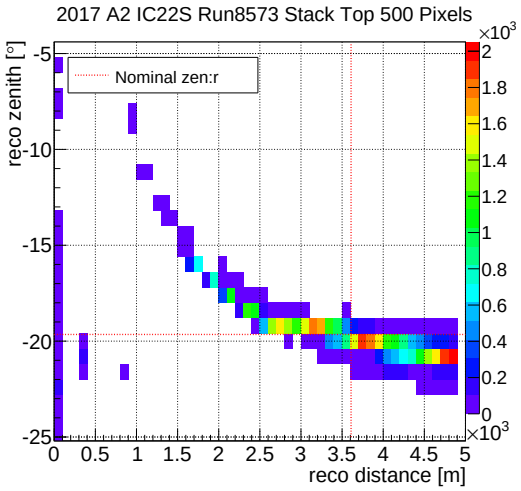

Figure 13: ARA-2 "stacked" pixels range vs. elevation(θ) distribution. Ranking by coherence values in decreasing order, we plot the (range, θ) of the highest 500 pixels of each event. Shown is this stacked distribution from events during time when ICS22 was pulsing. The color intensity scale indicates the frequency of a putative (range, θ) point.

summarizes our results numerically, and indicates that we can use the time difference be-

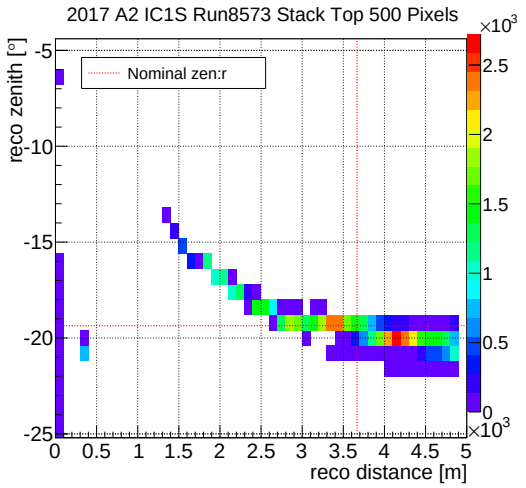

Figure 14: ARA-2 "stacked" highest 500 pixels range vs. elevation(θ) distribution during time when ICS1 was pulsing.

tween D and R signals to estimate the range to within ∼15%.

III. Study of H/V relative signal timing and evidence for birefringence

The pulses are emitted from a Vpol antenna and the Vpol response is evidently dominant; however, there is a ∼5–10% Hpol relative amplitude signal evident from Figures 4 and 5. This HPol response can, in principle, arise from (at least) three sources, in isolation or in combination:

- cross-talk at the electronics level between VPol and HPol DAQ electronics traces, and/or cross-polarized VPol response from a dominantly HPol receiver antenna, both of which should lead to observed H/V signals which are simultaneous in time. This is, however, inconsistent with observations of local in-ice VPol calibration pulser transmitter signals, at distances of approximately 30-50 meters from the receiver array, which show no evident HPol signals comparable to those observed here.
- intrinsic HPol source emission from a dominantly VPol deep pulser transmitter antenna (again inconsistent with local calibration pulser data).
- An ice-related effect, including:
  - Inclined conducting layers within the ice, which act as an *in situ* polarizer.
  - "circular" birefringence, for which the birefringence basis is Left Circular Polarization vs. Right Circular Polarization, and which could "rotate" a pure VPol signal at the source to a mixture of VPol and HPol, resulting in, on average, an equal admixture of VPol and HPol propagating signals. The actual relative strengths of the two components would roughly vary linearly with distance.
  - "linear" birefringence, in which the signal projects onto two (presumably perpendicular) propagation axes, referred to as the "ordinary" ("O", with a refractive index n_O and a 'fast' propagation velocity c_0/n_O, with c_0 the vacuum velocity of light) or "extraordinary" ("E", with a 'slow' propagation velocity c_0/n_E) axes. Upon arrival at the receiver, each of the O and E signals then project back onto the receiver antenna axis, resulting in an expected doublet of signals for both V or H, with amplitude dependent on the inclination angle of the underlying birefringent basis relative to "true" horizontal/vertical, and a separation time dependent on the $n_O - n_E$ difference.

Given that ice crystals are known to exhibit linear, but not circular birefringence[27], we consider the arrival of the HPol signals prior to the arrival of the VPol signals to be most plausibly explained by linear ice birefringence, although this requires some bulk ice crystal alignment. In the absence of any ice crystal directional asymmetry, one would expect the radio-frequency wavespeed to be uniform in all

	Nominal/Reconstructed		
Source	θ (deg)	ϕ (deg)	r (m) (deviation)
A2 IC1	-19.36/-20.09	259.99/257.6	3666/4215 (+15%)
A2 IC22	-19.65/-20.74	266.17/264.4	3609/4896 (+36%)
A3 IC1	-16.57/-18.21	230.77/231.7	4269/4711 (+10%)
A3 IC22S	-17.51/-18.84	234.95/235	4040/4298 (+6%)

Table 1: Summary of reconstructed deep pulser source locations compared with "known" source location.

directions. Isotropy of the Antarctic ice sheet is broken in two directions – vertically, due to the gradient in hydrostatic pressure with depth and resulting in a compressional stress on ice crystals, and horizontally, due to the local ice flow direction and resulting in a torsional strain, and therefore, a preferred axis laterally.

To calculate the magnitude of the birefringent asymmetry between H/V pairs in data, we must correct for the 2-3 meter shallower deployment depth of the H-pol antenna of the pair, leading to a timing correction $\delta_t^{corr} \approx n(z)\delta z(sin\theta_i)/c_0$, with δz the vertical separation of the HPol vs. VPol receivers, θ_i the ray incidence angle relative to the horizontal, $n(z)$ the local index-of-refraction, and c_0 the velocity of light in vacuum. After applying this correction, the calculated HPol advance relative to same-string VPol channels is summarized in Figure 15, for deep pulser stations observed in the TestBed, ARA-2 and ARA-3. In the Figure, the horizontal value corresponds to the i^{th} VPol receiver channel; the y-value gives the measured time difference, after correction, relative to the zero birefringence expectation, for the nearest HPol channel. The corrected H/V arrival time differences δ_t^{V-H} are of order 15–40 ns, with the TestBed asymmetries approximately half that of the ARA-2 and ARA-3 timing asymmetries, consistent with expectations given the smaller pathlength. We note that prior to the vertical-displacement correction described above, the ARA-2 and ARA-3 δ_t^{V-H} values are consistent with each other; after correction, the value of δ_t^{V-H}(ARA-3) is typically 15–20% smaller than for ARA-2, despite the fact that the propagation distance from the deep pulsers to the ARA-3 station is approximately 15% longer. A simple explanation for this is, of course, that the H-V pair vertical separations have been mis-tabulated by $\sim$1.5 meters. Alternately, in the birefringent model, this result may suggest that the vector from the deep pulsers to ARA-2 is more aligned with the underlying birefringent basis than ARA-3. Geometrically, the line from IC1 to ARA-2 is very nearly directly perpendicular to the horizontal ice flow direction; the line from IC1 to ARA-3 is offset by $\sim$30 degrees relative to that line.

i. Cross-checks

Aside from birefringence, the observed time delay between the arrival of the HPol vs. VPol signals could, in principle, be due to a difference in either the group delay response of the HPol quad slotted-cylinder receiver antennas relative to the VPol bicone antennas, a miscalibration of the cable delays of the HPol receiver antennas relative to the VPol antennas, or a source mechanism resulting in emission of HPol signal approximately 30 ns prior to VPol emission. The magnitude of the time asymmetry (30 ns) relative to typical 1–2 ns group (or cable miscalibration) delays strongly argues against the first of these possiblities. The uniformity of the observed H/V time delays in all the cases tested argues against the second of these hypotheses; the third should result in the same H/V time delay observed for all three

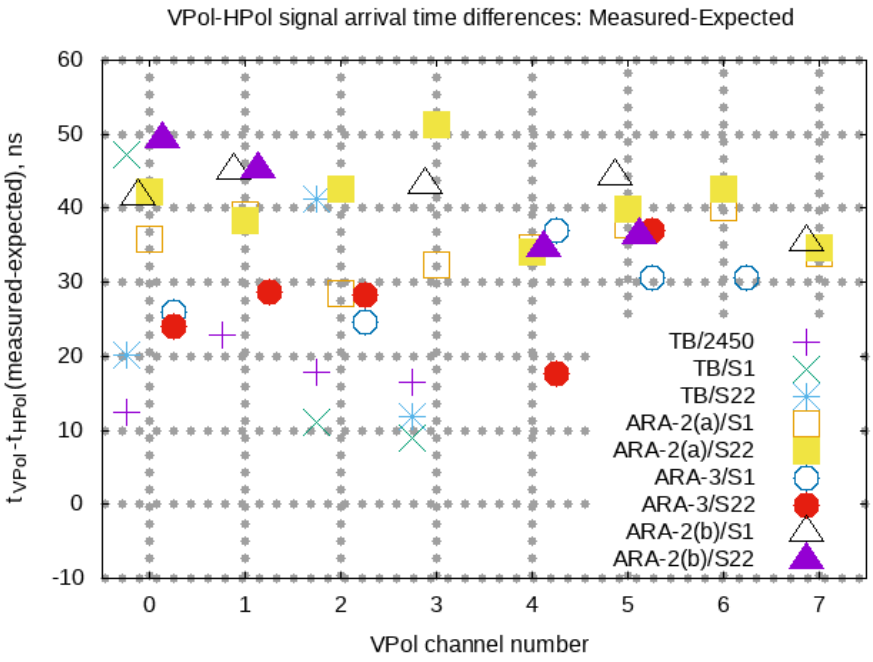

Figure 15: δ_t^{V-H} summary for TestBed, ARA-2 and ARA-3 data. x-axis refers to channel number of vertically-polarized receiver; y-value gives the (corrected) time difference between registered signal arrival time on the co-located VPol channel for that hole/station relative to registered HPol signal arrival time on the nearest HPol receiver. We observe that ARA-2 has typical time differences of 30-40 ns relative to a propagation time of approximately 20 μs; for ARA-3, values are approximately 5-10 ns smaller. Observed values for TestBed are somewhat lower than for both ARA-2 and also ARA-3, consistent with a measured δ_t^{V-H} proportional to pathlength. With the exception of TB/2450, remaining data are taken from 1400 meter deep pulsers. Per point estimated systematic errors are approximately 5 nanoseconds.

receiver stations, inconsistent with observation.

We nevertheless have attempted to exclude the possibility of timing mis-calibration directly from data. If there were a constant offset in the delays of all VPol vs. all HPol signals, then reconstruction of a source exclusively in VPol vs. exclusively in HPol would, of course, provide no information on a possible global timing offset between the two sets of receivers. We test the possibility of unaccounted-for timing delays (either cable or disparate group delays) by examining the characteristics of sources which give observable signals in both the VPol as well as the HPol channels, but also have pathlength through ice sufficiently short so as to render any possible birefringent effects unobservably small.

We have studied timing mis-calibration using Monte Carlo simulations, for which we can input any arbitrary timing offset between HPol and VPol. Simulations indicate that the VPol+HPol resolution in reconstruction of the source azimuthal coordinate should degrade by approximately a factor of three compared to VPol-only reconstruction, when there is a 40 ns calibration error in the former compared to the latter. By contrast, we find in fact, an improvement of ∼15% in the reconstructed azimuthal source precision for our VPol+HPol data sample, depending on the reconstruction algorithm used.

The channel-to-channel timing residuals offer an additional check of the HPol vs. VPol timing characteristics. Monte Carlo simulations of source reconstruction in the case of a 40 ns timing offset of HPol relative to VPol show an offset relative to zero, with magnitude half the timing offset, in the latter case (Fig. 16).

The reconstruction of signal in data (Fig. 17) is generally centered around zero residual for all channels, again arguing against a global timing mis-alignment between VPol and HPol channels. The horizontal width of the data distributions provides an estimate of the typical signal timing uncertainties.

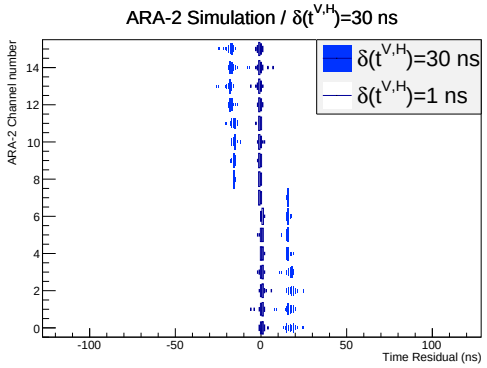

Figure 16: Time residuals vs. channel number, simulation; $\delta_t^{H,V}$=0 ns vs. $\delta_t^{H,V}$=40 ns

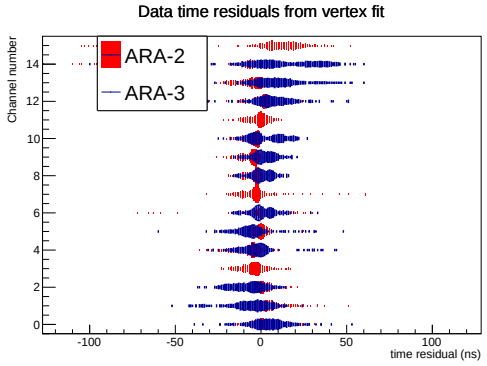

Figure 17: Time residuals vs. channel number, ARA-2 data. Channels 0–7 are VPol; channels 8–15 are HPol.

ii. Implications for birefringent alignment

Depending on the orientation of the birefringence basis with respect to the signal propagation k-vector and the signal polarization, the projection of signals emanating from a neutrino interaction onto the birefringent basis should result in a doublet of signals arriving simultaneously in both HPol as well as the VPol receiver channels, but with different relative amplitudes of the leading vs. lagging components of the pair. The fact that our data exhibit only one prominent signal in HPol and one in VPol suggests that, assuming birefringence, the birefringent 'vertical'-axis is aligned with the gravitational vertical z-axis.

IV. Conclusions and Discussion

ARA observations of the deep pulsers confirm the paradigm of geometric optics as the dominant mode for RF propagation through ice. As shown herein, the time difference between the direct and the refracted (or reflected) rays permits an estimate of the range-to-vertex, once the azimuth and elevation of an incident signal has been determined through interferometry. Additionally, if the time delay between signal arrival times for HPol vs. VPol receivers (δ_t^{V-H}) can be quantified for all geometries, then an additional constraint on the event geometry is afforded by the measured magnitude of birefringent time difference.

The evidence for birefringence must be interpreted in the context of previous results. The RICE Collaboration observed birefringence in vertical propagation of rays which reflect off the bedrock[25]. They conclude that the time delays accumulate mostly in the deep ice, below about 1200 m, as they observe no evidence for birefringence in the upper ice. This is consistent with a crystal orientation fabric (COF) determined by shear in the ice flow[20], which is rather modest in the upper ice. The current results, however, suggest that the upper ice does exhibit birefringence for horizontal propagation. If the COF of the upper ice is dominated by gravity, then a vertical ray would not exhibit birefringence, but a horizontal ray would since the Vpol would be along the net c-axis while Hpol would be transverse to it.

The observations presented here are a small part of the radio-glaciological data needed to fully characterize RF propagation of relevance to the ARA experiment. In this regard, within the last two years, a 1700-m deep ice core was extracted from the South Pole ice[23]. The data provided by that core, and its importance for neutrino detection, is currently under study by ARA. More importantly, the hole itself is located at distances of 0.5–several km from current and planned ARA stations, providing a unique opportunity to survey the ice as a function of depth and test RF propagation models against known ice characteristics. To this end, the ARA collaboration has been granted access to the SPICE hole for the 2017-18 and 2018-19 austral seasons, and are planning an extensive set of tests using transmitters lowered into that icehole. Key observations include investigation of a classical shadow zone due to the varying index of refraction, demonstration of horizontal propagation in the firn, and measurement of birefringence as a function of depth and incident angle. In addition to the deep ARA stations, data will also be collected by a surface station duplicating the ARIANNA design, but deployed at South Pole, providing data specific to horizontal propagation in the shallow firn.

V. Acknowledgments

We thank the National Science Foundation for their generous support through Grant NSF OPP-1002483 and Grant NSF OPP-1359535. We further thank the Taiwan National Science Councils Vanguard Program: NSC 102-2628-M-002-010 and the Belgian F.R.S.-FNRS Grant4.4508.01. We are grateful to the U.S. National Science Foundation-Office of Polar Programs and the U.S. National Science Foundation-Physics Division. We also thank the University of Wisconsin Alumni Research Foundation, the University of Maryland and the Ohio State University for their support. Fur-

thermore, we are grateful to the Raytheon Polar Services Corporation and the Antarctic Support Contractor, for field support. A. Connolly thanks the National Science Foundation for their support through CAREER award 1255557, and also the Ohio Supercomputer Center. K. Hoffman likewise thanks the National Science Foundation for their support through CAREER award 0847658. A. Connolly, H. Landsman, and D. Besson thank the United States-Israel Binational Science Foundation for their support through Grant 2012077. A. Connolly, A. Karle, and J. Kelley thank the National Science Foundation for the support through BIGDATA Grant 1250720. B. A. Clark thanks the National Science Foundation for support through the Graduate Research Fellowship Program Award DGE-1343012. D. Besson and A. Novikov acknowledge support from National Research Nuclear University MEPhi (Moscow Engineering Physics Institute). R. Nichol thanks the Leverhulme Trust for their support.

References

[1] G. Askaryan. Excess negative charge of an electron-photon shower and its coherent radio emission. *Soviet Physics JETP*, 14:441–443, 1962.

[2] G. A. Askaryan. Excess negative charge of electron-photon shower and the coherent radiation originating from it. radiorecording of showers under the ground and on the moon. *J. Phys. Soc. Japan*, Vol. 17, Suppl. A-III:257, 1962.

[3] G. A. Askaryan. Coherent radio emission from cosmic showers in air and in dense media. *Soviet Phys. JETP*, 21:658, 1965.

[4] Francis Halzen. High-energy neutrino astrophysics. *Nature Physics*, 13(3):232–238, 2017.

[5] Ralph Engel, David Seckel, and Todor Stanev. Neutrinos from propagation of ultrahigh energy protons. *Physical Review D*, 64(9):093010, 2001.

[6] Kumiko Kotera, Denis Allard, and Angela V Olinto. Cosmogenic neutrinos: parameter space and detectabilty from pev to zev. *Journal of Cosmology and Astroparticle Physics*, 2010(10):013, 2010.

[7] Markus Ahlers and Francis Halzen. Minimal cosmogenic neutrinos. *Physical Review D*, 86(8):083010, 2012.

[8] Katsuaki Asano and Peter MÃl'szÃąros. Ultrahigh-energy cosmic ray production by turbulence in gamma-ray burst jets and cosmogenic neutrinos. *Phys. Rev.*, D94(2):023005, 2016.

[9] P. Allison and J. Auffenberg and R. Bard and J. J. Beatty and D. Z. Besson and S. Boeser and C. Chen and P. Chen and A. Connolly and J. Davies and M. DuVernois and B. Fox and P. W. Gorham and E. W. Grashorn and K. Hanson and J. Haugen and K. Helbing and B. Hill and K. D. Hoffman and M. Huang and M. H. A. Huang and A. Ishihara and A. Karle and D. Kennedy and H. Landsman and A. Laundrie and T. C. Liu and L. Macchiarulo and K. Mase and T. Meures and R. Meyhandan and C. Miki and R. Morse and M. Newcomb and R. J. Nichol and K. Ratzlaff and M. Richman and L. Ritter and B. Rotter and P. Sandstrom and D. Seckel and J. Touart and G. S. Varner and M.-Z. Wang and C. Weaver and A. Wendorff and S. Yoshida and R. Young. Design and initial performance of the askaryan radio array prototype eev neutrino detector at the south pole. *Astroparticle Physics*, 35(7):457–477, 2012.

[10] P. Allison, J. Auffenberg, R. Bard, J. J. Beatty, D. Z. Besson, C. Bora, C.-C. Chen, P. Chen, A. Connolly, J. P. Davies, M. A. DuVernois, B. Fox, P. W. Gorham, K. Hanson, B. Hill, K. D. Hoffman, E. Hong, L.-C. Hu, A. Ishihara, A. Karle, J. Kelley, I. Kravchenko, H. Landsman, A. Laundrie, C.-J. Li, T. Liu, M.-Y. Lu, R. Maunu, K. Mase, T. Meures, C. Miki, J. Nam, R. J. Nichol, G. Nir, A. O'Murchadha, C. G.

Pfendner, K. Ratzlaff, M. Richman, B. Rotter, P. Sandstrom, D. Seckel, A. Shultz, J. Stockham, M. Stockham, M. Sullivan, J. Touart, H.-Y. Tu, G. S. Varner, S. Yoshida, and R. Young. First constraints on the ultra-high energy neutrino flux from a prototype station of the askaryan radio array. *Astroparticle Physics*, 70:62–80, 2015.

[11] P. Allison, R. Bard, J. J. Beatty, D. Z. Besson, C. Bora, C.-C. Chen, C.-H. Chen, P. Chen, A. Christenson, A. Connolly, J. Davies, M. Duvernois, B. Fox, R. Gaior, P. W. Gorham, K. Hanson, J. Haugen, B. Hill, K. D. Hoffman, E. Hong, S.-Y. Hsu, L. Hu, J.-J. Huang, M.-H. A. Huang, A. Ishihara, A. Karle, J. L. Kelley, D. Kennedy, I. Kravchenko, T. Kuwabara, H. Landsman, A. Laundrie, C.-J. Li, T. C. Liu, M.-Y. Lu, L. Macchiarulo, K. Mase, T. Meures, R. Meyhandan, C. Miki, R. Morse, J. Nam, R. J. Nichol, G. Nir, A. Novikov, A. O'Murchadha, C. Pfendner, K. Ratzlaff, M. Relich, M. Richman, L. Ritter, B. Rotter, P. Sandstrom, P. Schellin, A. Shultz, D. Seckel, Y.-S. Shiao, J. Stockham, M. Stockham, J. Touart, G. S. Varner, M.-Z. Wang, S.-H. Wang, Y. Yang, S. Yoshida, and R. Young. Performance of two Askaryan Radio Array stations and first results in the search for ultrahigh energy neutrinos. *Physical Review D*, 93(8):082003, 2016.

[12] AG Vieregg, K Bechtol, and A Romero-Wolf. A technique for detection of pev neutrinos using a phased radio array. *Journal of Cosmology and Astroparticle Physics*, 2016(02):005, 2016.

[13] S. W. Barwick and E. C. Berg and D. Z. Besson and E. Cheim and T. Duffin and J. C. Hanson and S. R. Klein and S. A. Kleinfelder and T. Prakash and M. Piasecki and K. Ratzlaff and C. Reed and M. Roumi and A. Samanta and T. Stezelberger and J. Tatar and J. Walker and R. Young and L. Zou. Design and Performance of the ARIANNA Hexagonal Radio Array Systems. *IEEE Trans. Nucl. Sci.*, 62(5):2202–2215, 2015.

[14] SW Barwick, DZ Besson, Alexander Burgman, E Chiem, Allan Hallgren, JC Hanson, SR Klein, SA Kleinfelder, A Nelles, C Persichilli, et al. Radio detection of air showers with the arianna experiment on the ross ice shelf. *Astroparticle Physics*, 90:50–68, 2017.

[15] P. W. Gorham, P. Allison, S W. Barwick, and et al. The Antarctic Impulsive Transient Antenna ultra-high energy neutrino detector: Design, performance, and sensitivity for the 2006-2007 balloon flight. *Astropart. Phys.*, 32(1):10 – 41, 2009.

[16] S Barwick, D Besson, P Gorham, and D Saltzberg. South polar in situ radio-frequency ice attenuation. *Journal of Glaciology*, 51(173):231–238, 2005.

[17] G de Q Robin. Velocity of radio waves in ice by means of a bore-hole interferometr1c technique. *Journal of Glaciology*, 15(73):151–159, 1975.

[18] Austin Kovacs, Anthony J Gow, and Rexford M Morey. A reassessment of the in-situ dielectric constant of polar firn. Technical report, COLD REGIONS RESEARCH AND ENGINEERING LAB HANOVER NH, 1993.

[19] Karl C. Kuivinen. A 237-meter ice core from south pole station. *Antarct J US*, 18(5):113–114, 1983.

[20] P Buford Price, Oleg V Nagornov, Ryan Bay, Dmitry Chirkin, Yudong He, Predrag Miocinovic, Austin Richards, Kurt Woschnagg, Bruce Koci, and Victor Zagorodnov. Temperature profile for glacial ice at the south pole: Implications for life in a nearby subglacial lake. *Proceedings of the National Academy of Sciences*, 99(12):7844–7847, 2002.

[21] S.H. Wang et al. Calibration, Performance, and Cosmic Ray Detection of ARIANNA-HCR Prototype Station. In *Proceedings*

of the 35th ICRC, Busan, Korea, volume 1, pages 1–8, 2017.

[22] Jordan Hanson. *The Performance and Initial Results of the ARIANNA Prototype*. PhD thesis, University of California, Irvine, July 2013.

[23] Kimberly Ann Casey, TJ Fudge, TA Neumann, EJ Steig, MGP Cavitte, and DD Blankenship. The 1500 m south pole ice core: recovering a 40 ka environmental record. *Annals of Glaciology*, 55(68):137–146, 2014.

[24] Ilya Kravchenko, David Besson, and Josh Meyers. In situ index-of-refraction measurements of the south polar firn with the rice detector. *Journal of Glaciology*, 50(171):522–532, 2004.

[25] Dave Besson, Ilya Kravchenko, Andres Ramos, and Juliet Remmers. Radio Frequency Birefringence in South Polar Ice and Implications for Neutrino Reconstruction. *Astropart. Phys.*, 34:755–768, 2011.

[26] M Beheler-Amass, M Beydler, A Karle, JL Kelley, and MY Lu. Interferometric neutrino event reconstruction in inhomogeneous media with the askaryan radio array. 1:1–8, 2017.

[27] ND Hargreaves. The radio-frequency birefringence of polar ice. *Journal of Glaciology*, 21(85):301–313, 1978.